A closer look to the mechanical behavior of the oxide layer in concrete reinforcement corrosion

B. Sanz , J. Planas , J.M. Sancho

A B S T R A C T

Results of concrete cracking in accelerated corrosion tests are presented for concrete prisms cast around a smooth steel tube simulating a rebar. Special instruments were used to measure the variation of inner diameter and volume of the tube while recording the width of the main crack by classical means. Numerical simulations of the tests with a model that reproduces the volumetric expansion of the oxide and the associated concrete cracking were used to narrow the uncertainties in the mechanical properties of the oxide layer with satisfactory results.

Keywords:
Cohesive crack
Accelerated corrosion tests
Reinforced concrete
Finite element modeling
Fracture mechanics

1. Introduction

Reinforced concrete structures exposed to aggressive environments often suffer corrosion of the reinforcing bars, due to the income of depassivating substances such as chlorides or carbon dioxide that break the passivity of the steel and lead to the generation of an oxide layer around the reinforcement. As a consequence, cracking of concrete occurs, since the oxide has a specific volume greater than that of the initial steel (Tuutti, 1982; Andrade et al., 1993; Alonso et al., 1998).

Since the pioneering work of Andrade et al. (1993) and Molina et al. (1993), much effort has been devoted, both experimental and numerical, to get better understanding of the cracking process and to find reliable models to describe concrete cracking due to reinforcement corrosion (Andrade et al., 1996; El Maaddawy and Soudki, 2003; Bhargava et al., 2006; Caré et al., 2007, 2008; Sánchez et al., 2010; Michel et al., 2011; Pease et al., 2012; Sanz et al., 2013). However, some of the basic properties of the oxide layer are still open to debate. The most influential is the expansion ratio of the oxide, which depends on the specific species of oxide formed (Tuutti, 1982; Mehta and Monteiro, 2006). Moreover, the *effective* expansion ratio may be less than that corresponding to a given species if the oxide or its precursors diffuse in the porous structure of the concrete (Molina et al., 1993). Expansion ratios of 2.0 are commonly used (Andrade et al., 1993; Molina et al., 1993; Sánchez et al., 2010; Michel et al., 2011), although higher values can also be found in the literature (Bhargava et al., 2006; Caré et al., 2008).

Even more uncertainty exists when the stiffness of the oxide layer is considered since direct in-place measurements, if feasible at all, are very difficult to perform. A wide range of values are found in the literature: in Molina et al. (1993), the bulk modulus of the oxide was taken to be of the same order of magnitude as the bulk modulus of water (around 2 GPa); in Caré et al. (2008) and Pease et al. (2012) the elastic modulus was estimated from a combination of analytical models and experiments in which the radial displacement in concrete was measured by image correlation techniques; the values obtained in these two studies are, however, very different: an elastic modulus of 0.14 GPa is reported in Caré et al. (2008), while the values of the elastic modulus reported in Pease et al. (2012) range between 2.0 and 20 GPa. The differences in the reported values can come from various sources. Some arise due to different conditions in the precise way in which corrosion takes place, for example, the current density and the availability of oxygen affect the type of oxide generated, and so, the properties of the oxide layer (Tuutti, 1982; Andrade et al., 1996). Some arise due to the simplifications assumed in the models used to infer the oxide properties from the direct measurements (for example, using a simplified specimen geometry, assuming a priori the path of the cracks, or not reproducing the actual boundary conditions of the experiments, among others). Finally, some oxide parameters might be inferred from experimental measurements having low

sensitivity to variations in those parameters. Whatever the exact sources of the discrepancy of the various published results, it seems clear that further research is necessary to narrow the uncertainties about the properties of the oxide.

Recently, the authors reported a work in which concrete prisms with an embedded steel tube — acting as a rebar — were subjected to accelerated corrosion, and the experimental crack pattern was compared to that predicted numerically, with good agreement (Sanz et al., 2013). To investigate corrosion-induced cracking, an interface element, called *expansive joint element*, was developed to simulate the volumetric expansion of oxide (Sanz et al., 2013); it works together with finite elements with an embedded adaptable cohesive crack (Sancho et al., 2007a), which describe fracture of concrete according to the basic cohesive model introduced by Hillerborg et al. (1976). In that type of tests, in which only the crack pattern is sought, the expansion factor is of little concern, since it affects only the time required to reach a prescribed crack width. But it was shown that to get realistic numerical results, a fluid-like behavior had to be assumed, as proposed by Molina et al. (1993), which was achieved by a strong reduction of the shear stiffness and of the tensile normal stiffness, while a change of the bulk modulus by a factor of 10 or 0.1 produced a change of the resulting crack opening of the order of only 5%.

In the present work, a novel set-up of accelerated corrosion tests is presented to characterize the cracking of concrete due to corrosion of the reinforcement. The specimens were, as in Sanz et al. (2013), concrete prisms with a smooth steel tube instead of a bar, equipped with instruments specially designed to measure the variation of inner diameter and volume of the tubes, while the width of the main crack across the concrete cover was recorded by standard means along the corrosion process, which was driven by the well known impressed current technique (Andrade et al., 1993; El Maaddawy and Soudki, 2003; Caré et al., 2007). Numerical simulations of the tests were carried out following the same procedures as previously used in Sanz et al. (2013). The model captured the main trends observed in the experiments and the measurements are sensitive enough to allow a substantial improvement in the indirect determination of the constitutive parameters of the oxide.

It should be noticed that the results presented in this work correspond to accelerated corrosion; since the density of current affect the type of oxide generated (Andrade et al., 1996), further experiments should be carried out in the future to determine the influence of the current density on the results and to determine the behavior of the oxide generated in the case of natural corrosion.

The paper is organized as follows: Section 2 describes the specimens, materials and experimental devices; Section 3 presents the experimental results; Section 4 briefly describes the numerical model and displays the results of the simulations and their comparison with the experimental results; finally, Section 5 reflects the main conclusions of the research.

2. Experimental method

2.1. Outline of the experiments

Specimens for concrete characterization and for accelerated corrosion tests were prepared from a single concrete batch. Six standard cylinders and four standard beams were cast for the determination of the fracture properties of concrete. Eight concrete prisms were cast with a calibrated steel tube as reinforcement to be tested in accelerated corrosion tests; for short, we call them TRP (tube-reinforced prism). The concrete mix proportions, specimen fabrication and results of the concrete characterization tests are given in Section 2.2.

The TRPs — see Fig. 1(a) and (b) — were designed to get a single main crack across the cover. The results in Sanz et al. (2013) proved that this was indeed the case, and that, although there were between four and five secondary cracks, their opening was much less than that of the main crack and none of them reached the surface of the specimen as schematically depicted in Fig. 1(c). The pattern was qualitatively the same in all the specimens, although the presence of aggregates locally modifies the crack path. Fig. 2 shows the pattern of cracking obtained for one of the specimens in this work, which was infiltrated with fluorescent resin and inspected under UV light (see Sanz et al., 2013 for the details of the impregnation technique). Nevertheless, other patterns and types of cracks are found for specimens with different geometries, as reported by Caré et al. (2010) and Nguyen et al. (2011) for mortar beams and plates. With regard to crack initiation, detailed simulations using 2D finite element models of specimens with the same geometry than the specimens of this work, but reinforced with a bar, showed that cracks initiate at the steel–concrete interface and propagate towards the outer surface of concrete (Sanz et al., 2013). However, there is an abrupt change in the crack opening profile when the main crack reaches the surface: the crack opening becomes suddenly larger at the surface than at the steel. This abrupt change occurs, however, for very small crack openings near the steel — less than 0.5 μm — and it was not possible to assess experimentally that the main crack does indeed grow initially from the bar towards the surface. The only direct information currently available about the crack pattern corresponds to the end of the test.

Special care was taken to provide impervious and electrically insulating coatings at the two extreme faces of the TRPs perpendicular to the axis of the tube to achieve electrical and displacement fields as plane as possible (since the planer the fields, the more accurate the two-dimensional simulations).

The eight TRPs were subjected to accelerated corrosion at a constant imposed electrical current in a temperature-controlled environment. In all the tests, the main CMOD (crack opening displacement for the main crack), electrical current, electrical potential difference, and the temperatures of the ambient, water-bath and specimen were continuously recorded as described in Sections 2.3 and 2.4. Half of the specimens were further instrumented with a specially designed diametral extensometer to measure the variation of the inner diameter of the tube, as described in Section 2.5. The other four specimens were instrumented with a capillary tube to measure the variation of the inner volume of the tube, as described in Section 2.6.

2.2. Materials and fabrication of specimens

All the specimens were cast from a single batch of a porous concrete fabricated in laboratory conditions with Portland Cement I 52.5 R, defined in the European Standard EN 197-1. Siliceous sand and aggregates with a maximum size of 8 mm were used, and a 3% of $CaCl_2$ by weight of cement was added to depassivate the steel; superplasticizer and set retarding admixture were also added to compensate for the accelerating effect of the calcium chloride. The mix proportions are displayed in Table 1 and are identical to those used in Sanz et al. (2013).

All the specimens were cast in steel molds, kept in the molds for 24 h in laboratory conditions, and then taken out of the molds and stored in a bath of lime saturated water in a temperature-controlled chamber at 20 °C until testing time.

Six standard cylinders (150 mm in diameter and 300 mm in length) and four standard beams (100 × 100 × 500 mm) were used to characterize the fracture behavior of concrete at the age of

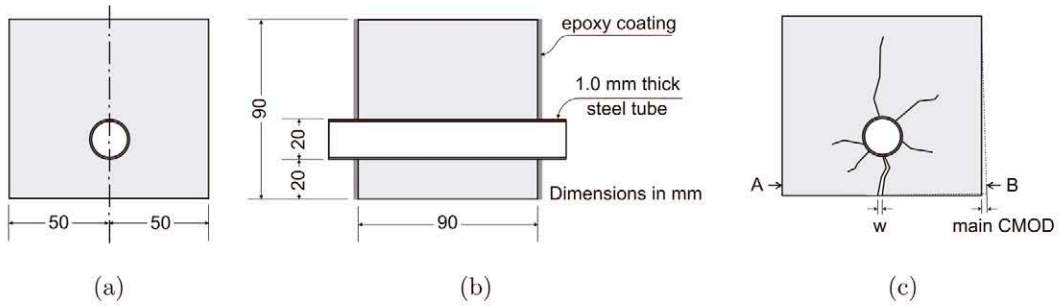

Fig. 1. Geometry of the specimens: cross-section (a); longitudinal section (b); sketch of crack pattern and of measured main CMOD (c).

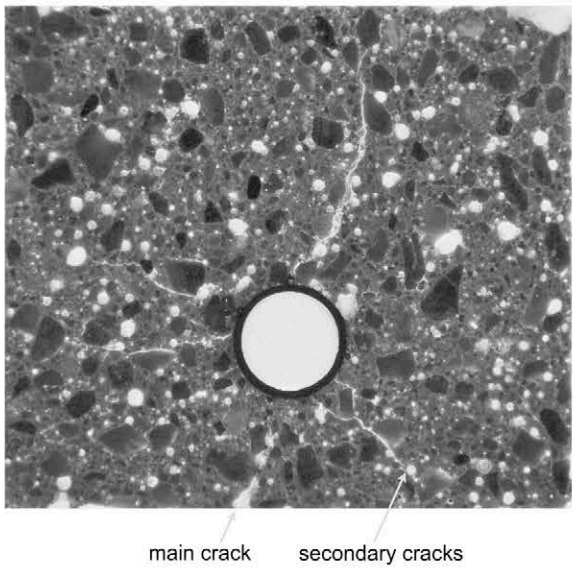

Fig. 2. Crack pattern obtained in accelerated corrosion tests.

Table 1
Concrete mix proportions, by weight.

Water	Cement	Sand	Agg.	$CaCl_2$	Set Ret.	Superplast.
0.5	1	2.85	2.05	0.03	0.01	0.0013

28 days. The results of the characterization test will be given in Section 4.1, where they are needed for simulation purposes.

Eight tube-reinforced prisms were cast from the concrete batch previously described. The reinforcing tubes were cut from seamless precision carbon steel tubes E-235 compliant with the EN 10305-1 standard. Their ends were machined to be normal to the axis and free of any visible defect. The procedure described by Kayafas (1980) was applied to clean the surface of the tubes, then an enamel coating was applied to both ends to prevent oxidization during casting and curing, while a central portion 80 mm in length was kept clean to adhere to concrete and free to corrode during the test.

After cleaning and insulation, the tubes were inserted in steel molds with the appropriate holes to hold the steel tube in place in a horizontal position and the concrete was poured in the molds and compacted in a vibrating table. As already indicated, the specimens were demolded after 24 h and stored in water at 20 °C until testing time.

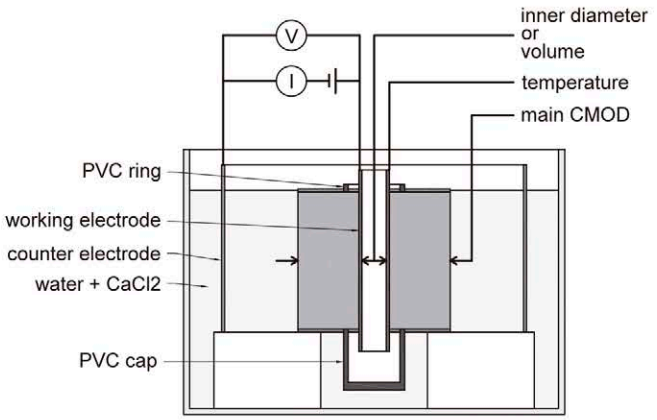

Fig. 3. Set-up of accelerated corrosion tests, elements for electrical insulation of the steel tubes and measurements during the tests.

2.3. Corrosion tests

During the test the specimen was placed, with the tube in vertical position, resting on four plastic supports inside an open plastic container, as shown in Fig. 3. The container was partially filled with water containing calcium chloride and a cylindrical stainless steel tube surrounding the specimen acted as the counter-electrode. The water level was adjusted to cover completely the lateral faces, but direct contact of the water and the tube was carefully avoided as described next.

After the curing period, the enamel coating was removed from the visible surfaces of steel, and, to provide electrical insulation and impermeability, the faces of the specimens perpendicular to the tube were coated with epoxy resin (top and bottom faces in the figure); the submerged end of the tube was also protected with a PVC cap bonded to the epoxy coating and a PVC ring was bonded to the top epoxy coating to protect the tube in case of slight variations in the water level. During the insulating process, the lateral sides of the prisms were covered with a wet sponge to avoid drying of the surface.

All the tests were instrumented with two type K thermocouples, one in the water bath and another attached to the end of the tube, and with a modified commercial strain gage extensometer to measure the main CMOD, which is described in the next subsection.

Two tests were run in parallel: one instrumented with a specially devised diametral strain gage extensometer, which measured the variations of the inner diameter of the steel tube and is described in Section 2.5, and the other instrumented with a capillary circuit to measure the variations of the inner volume of the tube, as described in Section 2.6.

After the instrumentation was complete, the specimens were placed in the bath and two constant-current sources were connected across the electrodes. The sources were designed to provide an adjustable current up to 20 mA, which were assessed to be stable within 0.07 mA when the resistance of the load circuit was reduced one order of magnitude.

All the tests were run under a constant current of 20 mA, equivalent to a current density of 400 $\mu A/cm^2$. This current density is, obviously, much higher than the values observed in real structures, which may affect the type of oxide generated (Andrade et al., 1996); however, it falls within the range 100–500 $\mu A/cm^2$ for which Faraday's law for steel dissolution has been shown to hold for chlorinated concrete (El Maaddawy and Soudki, 2003; Caré et al., 2007). Nevertheless, further work is in progress to investigate the influence of the current density on this kind of experiments.

To assure the efficacy of the insulation and the stability of the overall system, the first two tests were left running for over two weeks, until the imperviousness was finally lost and water found a path inside the tube, which happened after 18 days of uninterrupted corrosion. The remaining six tests were run for three days.

After accelerated corrosion, the loss of weight of the steel tubes corroded for three days was measured, following the procedure described in the ASTM G1 standard. It was compared to the theoretical gravimetric loss, which was calculated according to Faraday's law, assuming uniform corrosion along the tube. An efficiency of $100 \pm 9\%$ of the applied current was found.

Except for the level of the liquid in the capillary, all the measures were (nearly) continuously recorded using two 8-channel HBM Quantum MX-840 systems, namely, 5 temperatures (including the temperature of the room), 2 CMODs, 1 diametral variation, 2 current intensities and 2 voltage differences. In addition, pictures of the capillary were taken at regular intervals to measure (by visual post processing) the level of the liquid in the capillary. The details of the non-standard instruments are given next.

2.4. Main CMOD extensometer

A commercial MTS 632-11C-21 extensometer was adapted with horizontal and vertical extensions to measure the main CMOD at the central cross-section of the prisms, as depicted in Fig. 4. In particular, the extensometer measured the opening between the points labeled as *A* and *B*, which were located at 45 mm from the top surface and at 5 mm from the vertical face closest to the steel tube.

The extensometer was vertically supported by friction at the measuring points. The frictional force was increased by increasing the clamping forces at the supports — Fig. 4 — by means of an external spring-loaded stainless steel frame which, for clarity, is not shown in the figure. Special care was taken to avoid introducing any bending in the extensometer arms.

The extensometers were calibrated using an INSTRON high-magnification extensometer calibrator G55-1M and were found to have a linear range of 6.5 mm with linearity and proportional errors less than 0.7 μm and 2.2 μm, respectively, for ranges of calibration of 1000 μm.

It must be noted that the measured CMOD does not strictly correspond to the opening width *w* of the main crack at the surface of the concrete cover as sketched in Fig. 1(c), but to the relative displacement between the points of contact of the extensometer (points *A* and *B* in Fig. 4), which also includes contributions from the elastic deformation of the concrete and from the opening of the secondary cracks existing between those points, as depicted in Fig. 1(c), and that it was not measured exactly at the plane containing the mouth of the crack, but at 5 mm from it, due to physical restrictions to safely anchor the extensometer to the specimens. However, this setup had the benefit that the extensometer provided a continuous measurement of the main CMOD from the beginning of the test, independently of the position of the crack, and the measurement can be reproduced very easily in numerical simulations by recording the displacements of points *A* and *B* in the finite element model.

2.5. Diametral extensometers

A special extensometer was designed to measure the variation of inner diameter of the tubes during accelerated corrosion tests, since no commercial apparatuses were available to fit inside the tube. The active element is an elastic beam 0.2 mm thick, 5.5 mm wide and 10 mm long, made of a high strength aluminum alloy. The beam is monolithic with two 3 mm thick clamping ends; it was shaped using electric discharge machining of a $3 \times 6 \times 22$ mm aluminum block.

The extensometer functions as depicted in Fig. 5(a): the two ends of the beam are clamped to two independent rigid frames pushed against two diametrically opposed generators of the inner wall of the steel tube; when the diameter decreases by ΔD, the

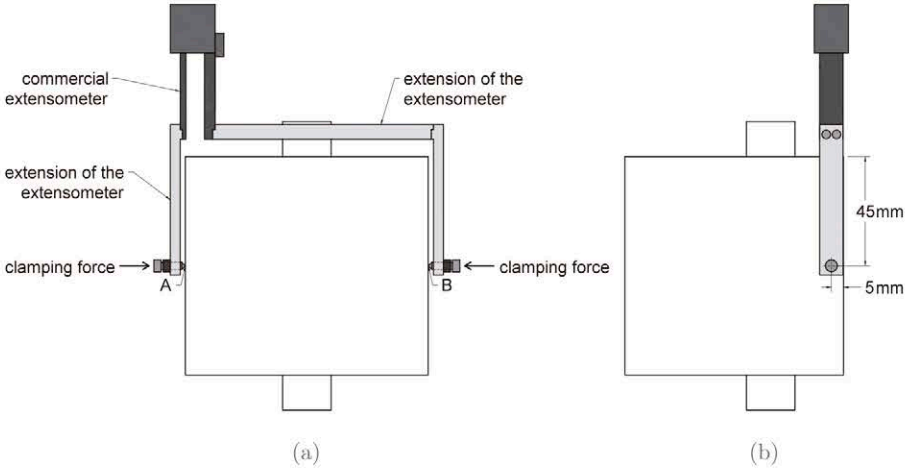

Fig. 4. Frontal (a) and lateral (b) views of a commercial extensometer adapted to measure the main CMOD at the middle section of the prisms, between the points *A* and *B*. For clarity, the spring-loaded stainless steel frame providing the clamping forces is not shown; neither is a horizontal tie attached at the extensometer case to provide rotational stability.

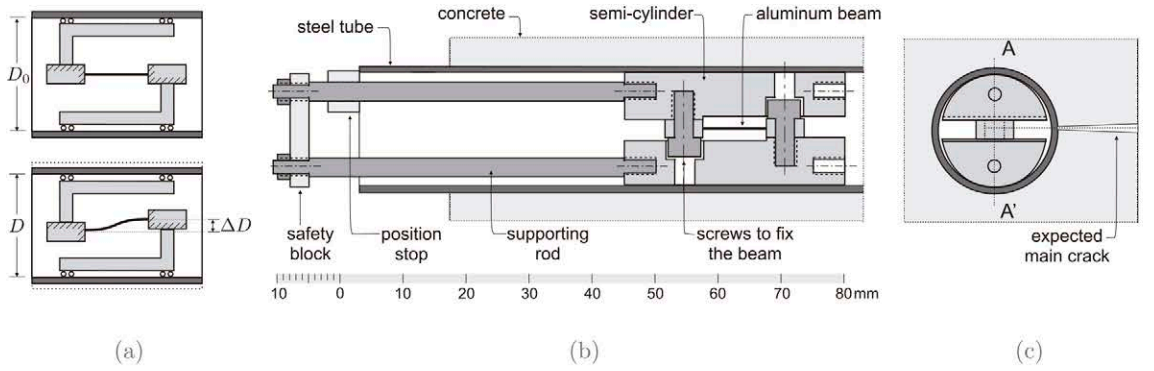

Fig. 5. Sketch of the functioning of the extensometers to measure variation of inner diameter (a), elements and accessories of the extensometer (b) and top view of the extensometer as placed in the experiments, to measure the diameter defined by AA' (c).

clamped ends of the beam suffer a relative parallel displacement, which leads to a double bending profile as shown in the figure. The bending is transformed into an electric signal by bonding four dual grid strain gages onto the faces of the beams, close to both ends. The eight strain gages are wired in a full bridge which captures the double bending and is insensitive to torsion and uniform bending.

In practice, the rigid frames consisted of two aluminum semi-cylinders complemented with a few additional elements to facilitate handling, as sketched in Fig. 5(b) and (c). The cylinders were machined to leave a gap of 0.5 mm between them, which provides a mechanical stop to avoid beam overloading; two handling rods were added that incorporate a position stop and a safety block to avoid extensometer damage during handling. The safety block is removed at the beginning of the test.

Six extensometers were fabricated that measured inner diameter ranging from 18.200 to 17.750 mm. They were calibrated with an INSTRON high-magnification extensometer calibrator G55-1M and were found to have a linear range of 450 μm with linear and proportionality errors less than 1.2 μm and 1.4 μm for ranges of calibration of 150 μm.

In the experiments, the extensometer was placed as depicted in Fig. 5(c), contacting the steel tube at the lines A and A' that define the diameter perpendicular to the expected main crack. Fig. 6 shows a top view of a fully instrumented specimen with the diametral extensometer in place.

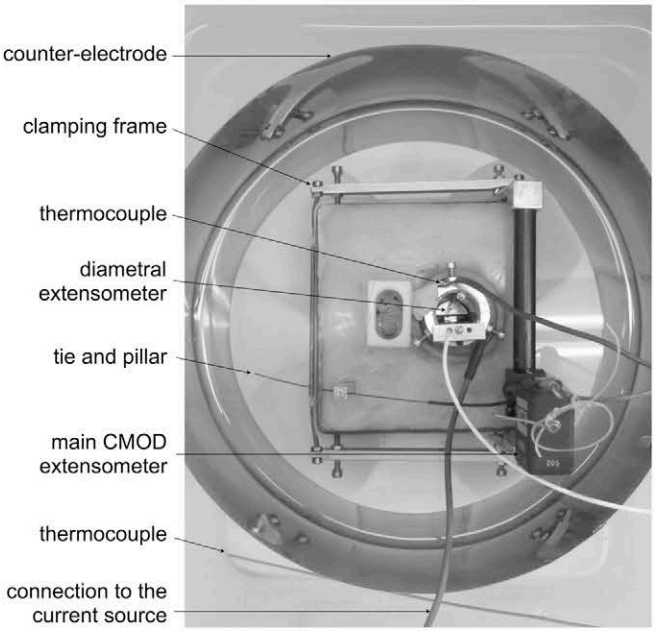

Fig. 6. Accelerated corrosion tests in a specimen with diametral extensometer.

2.6. Capillary circuit to measure variation of inner volume

The design of the capillary circuit to measure variation of inner volume of the steel tube is conceptually very simple: seal the two ends of the tube except for an exit through a capillary glass tube, fill the tube with a liquid, and record the variation of the level of the liquid in the capillary: such a variation is proportional to the variation of volume inside the tube. Unfortunately, the device turned out to be difficult to materialize and to handle, and a considerable effort was required to get reliable results. First, it was impossible to avoid trapped air bubbles by using simple gravity-driven filling of the liquid. Thus, the filling had to be carried out under vacuum. And second, since the thermal dilatation coefficient of the liquid is many times that of the steel, the device worked like a liquid-in-glass thermometer, and the capillary oscillations due to the small oscillations of temperature in the air-conditioning system (±1.25 °C) completely shadowed the variations of volume due to the mechanical deformation of the tube. This problem was handled by drastically reducing the volume of the fluid — filling most of the volume of the tube with a dummy steel plug — and by correcting the small remaining oscillations using the measured oscillations of temperature.

The final design is shown in Fig. 7: two reusable brass caps were used to seal the tube and a steel cylindrical plug with conical ends was inserted coaxially in the tube between the caps. The top cap had a three-way connection: one was the thick wall capillary glass, the second a metallic tube connected to the vacuum pump, and the third the filling conduit through which the liquid was let into the tube.

The glass capillary had an inner diameter of 0.508 mm; thus, a uniform reduction of 1.0 μm in the diameter of the steel tube would result in an increment of 11.16 mm in the level of liquid (calculated over the length of tube freely corroding, i.e., 80 mm). Silicone oil 350 cs was chosen to fill the circuit for being chemically inert and an electrical insulator.

An external frame lightened by a fluorescent lamp provided a reference for the measurement of the height of liquid in the capillary, as shown in Fig. 8(a).

Photographs were taken automatically at regular intervals. After the end of the tests the photographs were visually processed and the liquid level at the corresponding time was manually

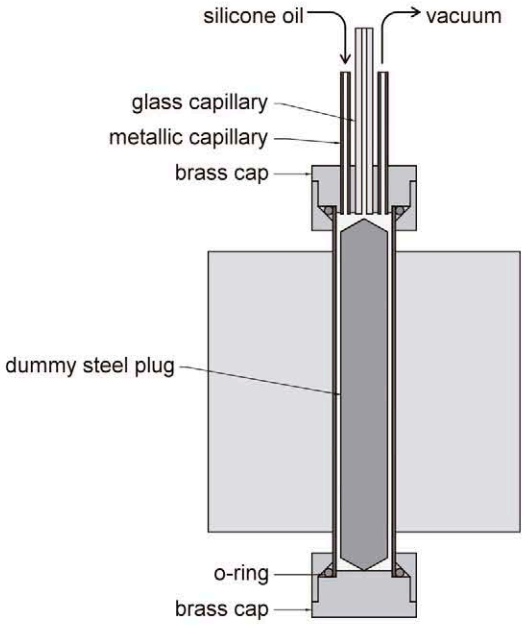

Fig. 7. Capillary circuit to measure variation of inner volume of the steel tubes in accelerated corrosion tests.

tabulated. Fig. 8(a) displays one of these pictures, which shows that the level of liquid in the capillary is clearly defined (the refractive index of the oil was such that the interior of the capillary appeared as white when empty and fully transparent when full of liquid, thus letting the dark background to be seen through it).

The device was calibrated on spare tubes to account for the thermal oscillations. It was found that an approximately linear relationship existed between the variation of the measured temperature and the observed variations of capillary height, but, since the changes of temperature of the liquid inside the tube were delayed with respect to those measured at its surface, as expected in unsteady heat-transfer problems, a simplified model with a constant shift time was used for the correction. Thus, the measured liquid height in the capillary at a given time t was corrected using the formula

$$H(t) = H_m(t) - m\Delta T_m(t-\tau) \tag{1}$$

in which $H_m(t)$ stands for the capillary height measured at time t and $\Delta T_m(t-\tau)$ for the temperature variation measured τ seconds before t; m is the proportionality constant and τ the shift time, which, in the calibration tests, were determined to be $m = 29$ mm/°C and $\tau = 450$ s. Fig. 8(b) shows a picture of a fully instrumented test including the capillary circuit.

3. Results of the accelerated corrosion tests

After the tests, the corrosion depth x was calculated for each specimen from the record of intensity I versus time using Faraday's law, assuming perfect effectiveness of the current and uniform corrosion along the tube, which results in

$$x(t) = \frac{M_m}{\rho S z F}\int_0^t I(t')dt' \tag{2}$$

where $x(t)$ is the corrosion depth at time t, $M_m = 55.8$ g/mol the molar mass of iron, $\rho = 7.85$ g/cm^3 the iron density, $S = 50.27$ cm^2 the area of the corroding surface, $z = 2$ the valence number of iron ions (assuming that Fe^{2+} ions are generated during the process), $F = 96.49$ kA s/mol the Faraday constant, and $I(t')$ the measured current at time t'. With the given data, this reduces to

$$x = k\int_0^t I(t')dt', \quad \text{with} \quad k = 7.33\ 10^{-6}\,\frac{\mu m}{mA\ s} \tag{3}$$

which gives a final corrosion depth of 38 μm after 3 days for an imposed current of 20 mA. The integral was computed numerically for each specimen using Simpson's rule.

To account for the small variations in electrical current the measured difference of potential V was converted to the nominal potential V^* corresponding to a nominal intensity $I^* = 20$ mA with the expression

$$V^* = V\frac{I^*}{I} \tag{4}$$

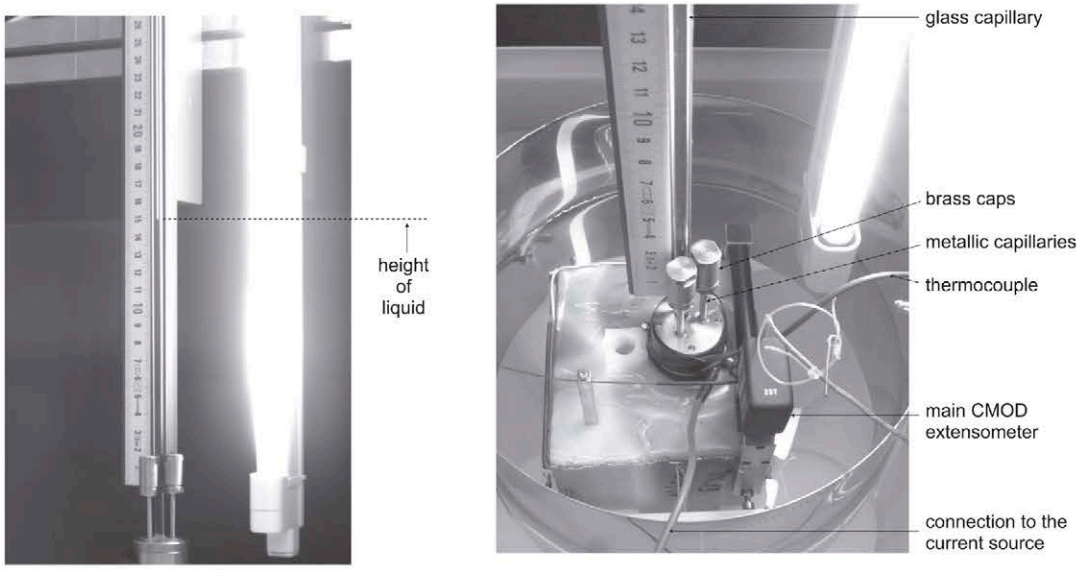

Fig. 8. Example of one of the photographs from which the liquid height in the capillary was visually read (a), and view of a specimen fully instrumented with a capillary circuit (b).

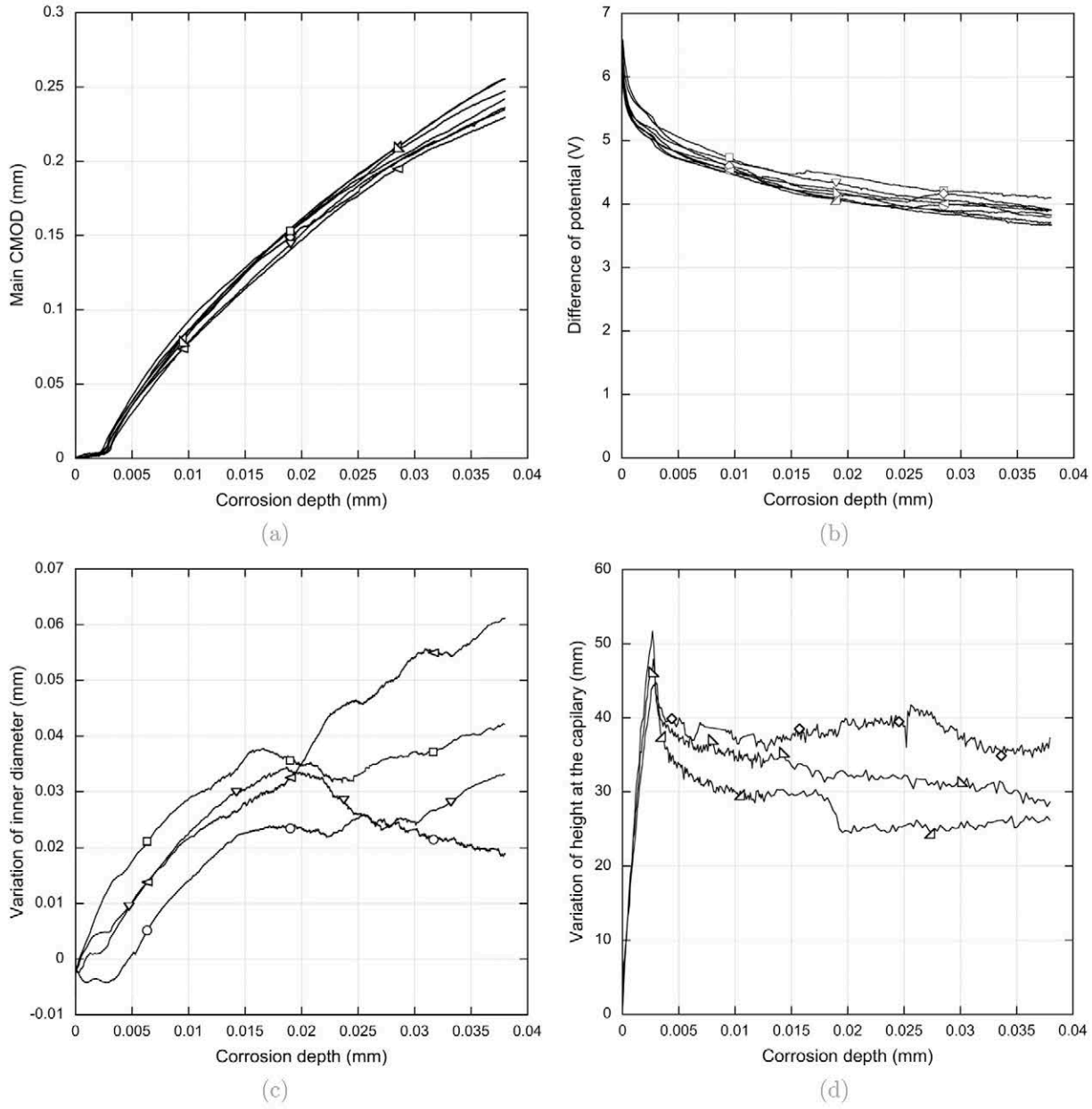

Fig. 9. Curves of variation of main CMOD (a), nominal difference of potential (b), variation of inner diameter (c), and variation of liquid height in the capillary (d) versus corrosion depth, obtained in accelerated corrosion tests with a current density of 400 $\mu A/cm^2$ for 3 days.

Finally, the readings of capillary height were corrected for the effect of temperature oscillations using Eq. (1), and the variations of capillary height, inner diameter and main CMOD were plotted versus the corrosion depth x.

Fig. 9 displays the corresponding plots for all tested specimens. For the two tests lasting more than 3 days, the curves were plotted up to a corrosion depth of 38 μm, corresponding to the duration of the other tests. The results of main CMOD and of liquid height in the capillary of one of the specimens had to be discarded due to slippage of the CMOD extensometer and leakage in the capillary circuit, respectively.

In all the specimens, a main crack developed through the cover, as expected. The main CMOD — Fig. 9(a) — grew very slowly during the first few microns of corrosion depth but at a depth of about 2.5 μm the slope of the curves increased abruptly, which is a clear indication of the formation of the main crack through the cover, which will be called the *break-point* in the following. From this point on, the slope of the curves decreases smoothly and a mean opening of 244 μm is achieved for a corrosion depth of 38 μm. This decrease in the slope will be discussed in Section 4.3, and might be due to a diminution in the *effective* expansion ratio of the oxide, due to diffusion, although no attempt has been made in this work to quantify this effect. The scatter for this measurement is relatively small in these tests.

The difference of electrical potential — Fig. 9(b) — continuously decreased during accelerated corrosion, indicating a reduction in the electrical resistance of the specimens. The curves show a steeper decrease at the beginning, and a further steeper slope at a corrosion depth coinciding very approximately with the break-point detected in the CMOD-x curves.

The curves of variation of inner diameter — Fig. 9(c) — show a high scatter, but they all have an overall trend to grow with the corrosion depth, except for a slight decrease (less than 4 μm) at the beginning of the test, probably until the first crack appears.

The curves of variation of liquid height in the capillary — Fig. 9(d) — display a steep rise during the first microns of corrosion depth, up to a peak that coincides with the initiation of cracking in the curves of main CMOD. The peak is followed by a relatively small, but steep, decrease, followed by a slowly decreasing tail. That means that there was a reduction of inner volume until the initiation of cracking and then it partially recovered although there was a remaining diminution of volume.

The difference in the trend displayed by the curves of inner diameter and capillary height can be explained by a change in the shape of the cross-section of the tube from circular to oval. Indeed the variation of liquid height at the peak (48.1 mm) would correspond to a uniform reduction of 4.31 μm in the inner diameter of the tube, while the variation of diameter is positive, on average. After the peak the inner volume keeps being less than the initial one, while the inner diameter grows continuously up to about 40 μm, on average; this can only be explained if a diameter perpendicular to the one we measure *decreases* by an amount slightly larger than the measured increase so that the sum of the increases of the two perpendicular diameters is small and negative (the few microns required to accommodate the measured decrease in volume). The dissimilar behavior is qualitatively easy to understand: the opening of the main crack strongly reduces the internal stresses that tend to compress the tube in direction normal to the crack, while the stresses parallel to the main crack are much less relieved.

Table 2 shows the mean and the standard deviation of the significant points in the curves of main CMOD and variation of liquid height in the capillary and the final values for all the curves. The break point in the curve of main CMOD had a standard deviation larger than the peak in the curve of variation of capillary height, because the break in the first curve was softer than the peak in the second one, although they occurred at the same average corrosion depth, which will be called the *critical corrosion depth* $x_c := x_{break} = x_{peak}$. For the values at the end of the tests for a corrosion depth of 38 μm, the standard deviation was of the same order than those in the fracture parameters of concrete (see Table 3), thus, the difference between the curves may be explained by the heterogeneity of the fracture process itself, except for the curves of inner diameter; for these, other factors may affect the results, especially the position of the measured diameter with respect to the main crack, which, in a sense, controls the asymmetry of the deformation of the tube.

Table 2
Results of accelerated corrosion tests: break in the curves of main CMOD versus corrosion depth $w_{break} - x_{break}$, peak in the curves of variation of liquid height in the capillary $\Delta H_{peak} - x_{peak}$, and final values for a corrosion depth of 38 μm of main CMOD w_{38}, nominal difference of potential V^*_{38}, variation of inner diameter ΔD_{38} and variation of capillary height ΔH_{38}.

	w_{break} (μm)	x_{break} (μm)	ΔH_{peak} (mm)	x_{peak} (μm)	w_{38} (μm)	V^*_{38} (V)	ΔD_{38} (μm)	ΔH_{38} (mm)
Mean	5.43	2.64	48.1	2.76	244	3.85	39	30.7
Std. dev.	0.92	0.33	3.5	0.12	10	0.13	18	5.8

Table 3
Fracture parameters of concrete: mean and standard deviation of compressive strength f_c, tensile strength f_t, elastic modulus E, fracture energy G_F, mean horizontal intercept of the initial branch w_1 and stress at the kink point of the bilinear softening curve.

	f_c (MPa)	f_t (MPa)	E (GPa)	G_F (N/m)	w_1 (mm)	σ_k (MPa)
Mean	48.8	2.78	36.1	106.9	0.0430	0.322
Std. dev.	1.6	0.42	1.7	4.9	–	–

4. Numerical simulations

4.1. Outline of the model

Simulations of the tests were carried out using the model presented in Sanz et al. (2013) that reproduces fracture of concrete and expansion of oxide as described next:

Fracture of concrete is described according to the standard cohesive model, introduced by Hillerborg et al. (1976), which assumes that when a crack appears, it transmits stresses at its faces following a *softening curve* that is a scalar function of the opening of the crack, as schematically depicted in Fig. 10. To characterize the fracture behavior, three compression tests, three diagonal compression (Brazilian) tests, and four three-point bending tests on notched beams were carried out following the procedures described in Standards ASTM C39, ASTM C496 and Planas et al. (2007). Details of the model can be found in Bazant and Planas (1998), Elices et al. (2002) and Planas et al. (2003), and the bases of the experimental method in Guinea et al. (1994), Planas et al. (1999) and Fathy et al. (2008). The compressive strength and the fracture parameters of the concrete determined in those tests are shown in Table 3.

To reproduce the cohesive behavior of concrete, finite elements with an embedded cohesive crack are used (Sancho et al., 2007a,b), which are implemented within the finite element framework COFE (*Continuum Oriented Finite Elements*). They are constant strain triangles with strong discontinuity kinematics and central force model for the crack, as depicted in Fig. 11(a). In those elements, the path of the crack is not predefined, i.e., a crack can develop in any element and in any direction, depending on the local stress fields, and once a crack forms, it can reorient to adapt itself to the stress fields, until a threshold crack opening w_{th} is reached; once the threshold is attained, the orientation of the crack remains fixed. The threshold is defined by an adaptation factor α' as

$$w_{th} = \alpha' w_1 \tag{5}$$

where w_1 is defined in Fig. 10, and α' is of the order of 0.2 (Sancho et al., 2007a).

To simulate the volumetric expansion of the oxide, *expansive joint elements* were used at the steel–concrete interface (Sanz et al., 2013). These are four-node elements with zero initial thickness and elastic behavior that reproduce the expansion of oxide as a free expansion perpendicular to the initial surface of the steel and with a value equal to βx, where x is the corrosion depth, i.e., the amount of steel that is transformed into oxide, and β is the expansion factor of oxide, which is related to the specific volumes of steel v_{st} and oxide v_{ox} as

$$\beta = \frac{v_{ox}}{v_{st}} - 1 \tag{6}$$

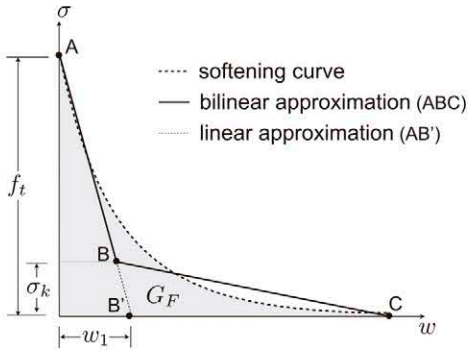

Fig. 10. Softening curve of concrete, according to the standard cohesive model, and linear and bilinear approximations of it.

According to this model, the traction vector $\mathbf{t}$ acting on an element for a given expansion βx and a mechanical displacement $\mathbf{w}$, is calculated as:

$$\mathbf{t} = \eta k_n(\mathbf{w}\cdot\mathbf{n} - \beta x)\mathbf{n} + k_t[\mathbf{w} - (\mathbf{w}\cdot\mathbf{n})\mathbf{n}] \tag{7}$$

where $\mathbf{n}$ is the initial unit normal to the element; in this simple model, ηk_n is the normal stiffness and k_t the shear stiffness. Obviously, the free expansion occurs at $\mathbf{w} = \beta x\mathbf{n}$, for which $\mathbf{t} = \mathbf{0}$.

To simulate a fluid-like behavior, the shear stiffness k_t of the element is taken to be much less than the normal stiffness k_n, and the factor η in the normal stiffness is introduced to simulate the expected debonding behavior when the normal stress is tensile; thus, η is taken to be equal to 1.0 in compression and a given factor $\eta_t \ll 1.0$ in tension.

A simplification is made in the finite element model to avoid remeshing, as depicted in Fig. 11(b): in the simulated section, the thickness of steel is kept constant, instead of eliminating from it the corroded layer. Thus, the thickness of 'equivalent oxide' in the interface element is strictly the net volumetric expansion βx, instead of $x(\beta + 1)$. To maintain mechanical equivalence of the real and simulated systems, the equivalent stiffnesses of the interface element are calculated, based on the properties of the steel and the real oxide for each corrosion depth. The basic result is that, as it might be expected, the stiffness of the oxide layer is inversely proportional to the corrosion depth, which would require an infinite initial stiffness in the element. Since this is not acceptable in the ordinary formulation of the finite element method, a large, but finite, initial stiffness must be used. Therefore, numerical cut-offs k_n^0 and k_t^0 of the normal and shear stiffnesses are set for corrosion depths less than a given value x_0. See Sanz et al. (2008) and Sanz et al. (2013) for the details of the formulation of the model. The specific values for these and the remaining parameters of the simulations are given next.

4.2. Parameters used in the simulations

Simulations of the tests were carried out on 2D FE models of the concrete prisms described in Section 2.2, with a steel tube as a reinforcement.

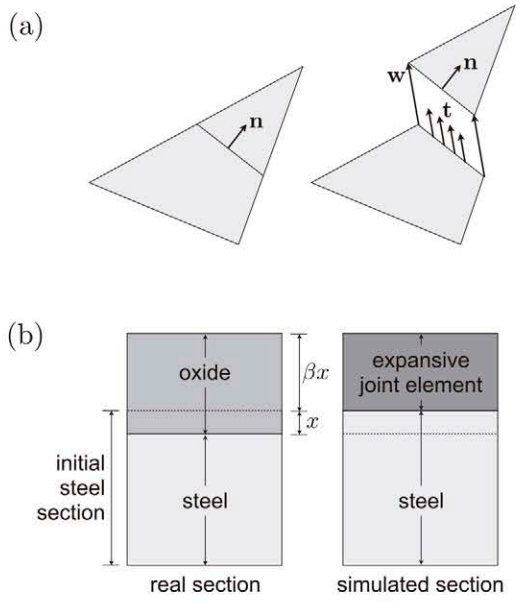

Fig. 11. Finite elements with an embedded adaptable cohesive crack were used for the concrete (a), and expansive joint elements reproduced the volumetric expansion of oxide βx for a given corrosion depth x (b).

The mesh was generated using the finite element mesh generator *Gmsh*, distributed under the GNU General Public License (Geuzaine and Remacle, 2009). Constant strain triangles were used for the concrete, while for the steel quadrilateral elements with assumed enhanced strains were chosen to get a better response in bending. The size of the quadrilateral elements was selected to adequately capturing the bending of the tube; a set of numerical tests with 1 to 5 elements in the thickness and 8 to 32 elements in a quarter of circumference were run and it was found that for 3 or more elements in the thickness and 16 elements and over per quarter circumference the differences were negligible, and, thus, a mesh with 3 quadrilaterals in the thickness and 16 per quarter circumference was selected, as shown in Fig. 12(a). The mesh in the concrete was generated to match the mesh in the tube and the size of the elements was linearly increased to be 5 times larger on the outer boundary of the specimen.

The boundary conditions of the problem were two simple supports at the two top corners of the concrete section. Two nodes were located in the same position than the measurement points of the main CMOD extensometer and their displacement was recorded. Finally, the displacements of all the nodes at the inner boundary of the steel tube were recorded. Fig. 12(a) shows the mesh, the boundary conditions and the position of the measuring points.

The computations were driven by the corrosion depth x, for which the free radial expansion βx was computed. A total corrosion depth of 20 μm was applied in 40 steps, which was smaller than the experimental corrosion depth, due to a computational limitation: when the numerical crack tip approaches a free surface in bending mode, as happens with the longest secondary crack, it tends to curl over itself and to block due to excessive gradients. Table 4 shows the parameters of the materials. For the steel, linear elastic behavior and standard values were assumed. For the concrete, the parameters were those obtained in the experiments described in Section 4.1, which, for the readers convenience, have also been included in Table 4. Note that the fracture energy of the linear curve is approximately half of the actual fracture energy.

For the expansive joint element, two sets of values were used, which have been labeled as *Oxide* 1, and *Oxide* 2. The first set of parameters is identical to that previously used in Sanz et al. (2013), based on a fluid-like behavior and a net expansion factor $\beta = 1.0$ as suggested in Molina et al. (1993), with very small shear and tensile stiffnesses. From the comparison of the numerical an experimental results for the main crack opening it became obvious first that the net expansion factor had to be doubled to get a good fitting; this expansion factor corresponds to an actual expansion ratio (v_{ox}/v_{st}) equal to 3.0, according to Eq. (6), which lies within the theoretical expansion ratio reported in the literature for various species of oxides (Tuutti, 1982; Mehta and Monteiro, 2006). And second, a less drastic reduction of the shear stiffness of the oxide layer further improved some of the results, particularly the volume change, which might be explained by the fact that although the oxide has a fluid-like behavior, and, thus, its shear stiffness is less than the normal stiffness, it still transmits stresses in that direction. No mathematical optimization was attempted, because of the large scatter in the experiments and the drastic simplifications in the oxide model. The parameters were selected based on computations with the linear softening, and then, final computations were carried out with the bilinear softening and with the two sets of parameters, which further improved the numerical results, as described next.

4.3. Results

Fig. 12(b)–(d) shows the comparison of the experimental results (gray lines) with the various numerical results (black lines). The

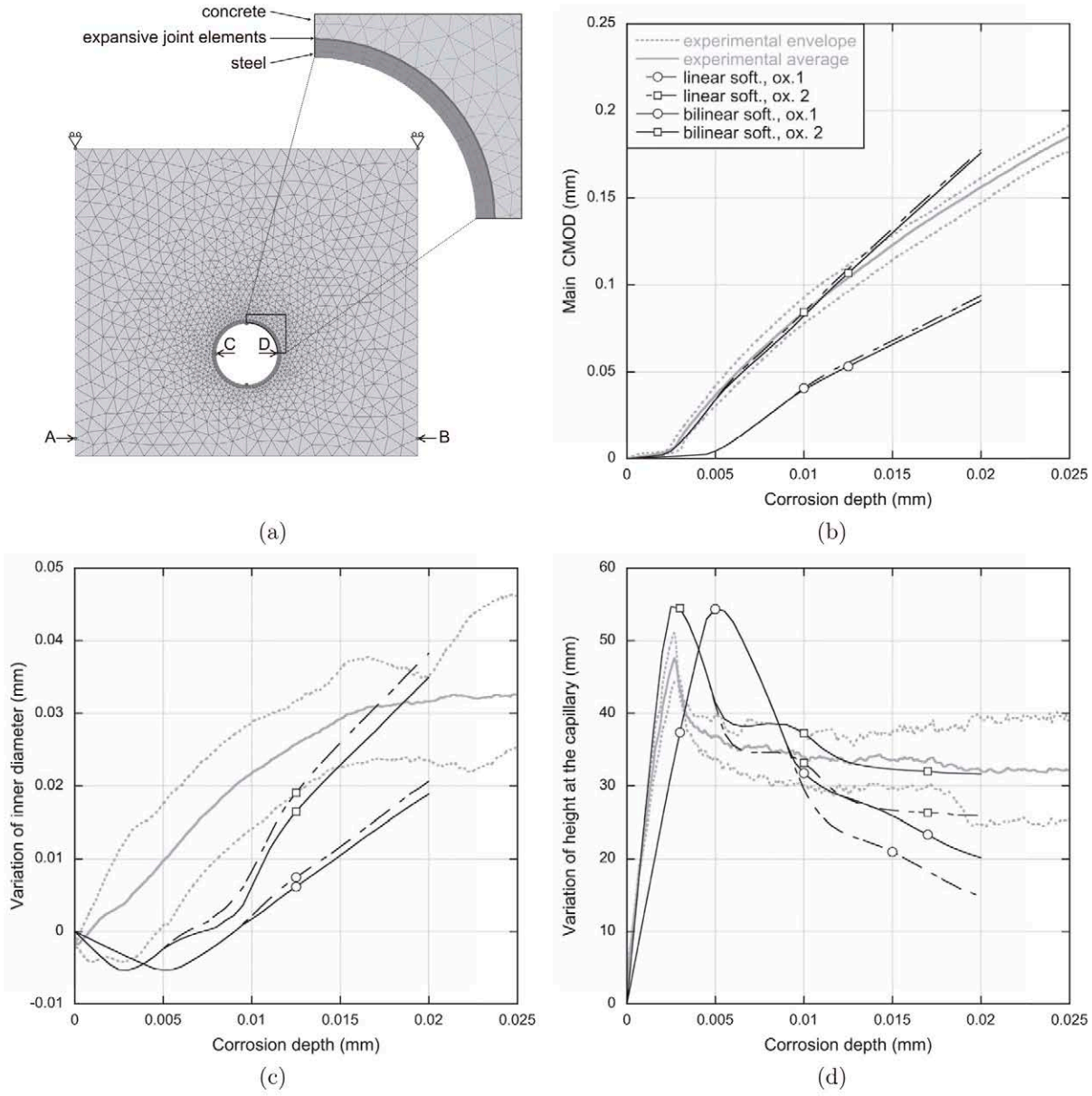

Fig. 12. Mesh used in the simulations (a) and curves of variation of main CMOD (b), variation of inner diameter (c) and variation of liquid height in the capillary (d) versus corrosion depth, obtained in numerical simulations with the expansive joint element.

Table 4
Parameters of the materials in the simulations, where E is the elastic modulus, ν is Poisson's ratio, f_t is the tensile strength, G_F is the fracture energy below the softening curve, w_1 is the intercept of the first branch of the softening curve with the abscissas axis, σ_k is the stress at the kink point, α' is the adaptation factor of the crack, β is the volumetric expansion factor, x_0 is the cut-off corrosion depth, k_n^0 and k_t^0 are the cut-off normal and shear stiffnesses and η_t is the reduction factor of the normal stiffness in tension.

	E (GPa)	ν	f_t (MPa)	G_F (N/m)	w_1 (mm)	σ_k (MPa)	α'
Steel	200	0.3	–	–	–	–	–
Concrete: linear soft.	36.14	0.2	2.780	59.7	0.0430	–	0.2
Bilinear soft.	36.14	0.2	2.780	106.9	0.0430	0.322	0.2
	β	x_0 (mm)	k_n^0 (N/mm^3)	k_t^0/k_n^0	η_t		
Oxide 1	1.0	1.0×10^{-3}	1.0×10^{6}	1.0×10^{-20}	1.0×10^{-11}		
Oxide 2	2.0	1.0×10^{-3}	1.0×10^{6}	1.0×10^{-3}	1.0×10^{-11}		

numerical curves corresponding to the bilinear softening are drawn as solid lines, while the dotted lines correspond to linear softening. The curves marked with a circle correspond to the set of parameters defined as *Oxide* 1, and those marked with a square to the set corresponding to *Oxide* 2.

Fig. 12(b) compares the experimental main crack opening with the corresponding numerical results, computed as the relative displacement between points A and B in the finite element mesh — Fig. 12(a). The numerical response is chiefly controlled by β (increasing β by a factor of 2.0 roughly decreases the abscissa of

the response curve by the same factor) while the influence of the shear modulus is much less noticeable as well as the influence of the tail of the softening curve (linear versus bilinear curve). The fit for *Oxide* 2 is quite good, specially for main crack openings up to about 100 μm. For larger crack openings the numerical response is nearly linear, while the experimental curve is clearly parabolic; this might be due to a time-dependent effect coming from diffusion of the oxide through the capillary network of the concrete, which would progressively decrease the effective expansion factor β, a possibility pointed out in the introduction based on previous published suggestions (Molina et al., 1993); a further possibility, is the migration of part of the oxide through the newly formed crack itself, a phenomenon that was documented experimentally by the authors in Sanz et al. (2013). Regarding the break point, which marks the localization of the main crack through the cover, in the simulations with *Oxide* 2, it is situated at the right x-position, but the kink is less abrupt than in the experiments.

Fig. 12(d) compares the experimental results for the variation of the liquid height in the capillary with the computed counterpart. The numerical value was obtained from the nodal displacements of the inner surface of the tube from which the variation of the area of the inner cross section was computed; the variation of volume was calculated by assuming a uniform deformation along the axis of the tube over an effective length equal to the unprotected length of the tube (the part free to corrode), i.e., 80 mm; the variation of the height in the capillary trivially followed. The numerical results for *Oxide* 1 capture the main trends seen in the experimental results: a fast rise up to a peak followed by a slower descent, but the initial rise is too slow, the peak exceeds the experimental one by 10%, approximately, and is located much too far along the x axis, the peak is much wider than the experimental one, and the tail goes down to values well below the experimental range. The increase in the expansion factor β and in the shear stiffness — *Oxide* 2 data set — sensibly improves the results: the initial slope does fit the results, the x-position of the peak is correct (it equals the experimental critical corrosion depth), and the post peak tail is raised and lies within the experimental band. However, the peak still overshoots the experimental one by about 10% and is much wider in the numerical curve, which is in correspondence with the previous observation that the kink in the main crack opening curve is less abrupt in the numerical results than in the experiments; the curve of capillary height is just much more sensitive to this phenomenon, which calls for further improvements in the numerical simulations. It should be noticed that the capillary height is also more sensitive to the shear stiffness and to the tail of the softening curve than the main crack opening. The error in the peak might be explained by the strength and the fracture energy of concrete in the computations being larger than in the specimens, since the numerical response has been computed based on the results of independent mechanical tests, and there are obvious differences between those and the accelerated corrosion tests, chiefly the crack opening rate, which is much faster in the characterization tests (see Bazant and Gettu, 1992; Bazant and Planas, 1998 for an explanation of the effect of the CMOD rate on the fracture parameters of concrete); in independent calculations it has been assessed that a reduction in the tensile strength and in the fracture energy of concrete less than 10% brings the peak down and narrows the peak width in the curves of capillary height; however, no attempt has been made in this paper to 'correct' the data and to take into account the differences between both kinds of tests.

Fig. 12(c) compares the experimental results for the variation of the inner diameter with the numerical results, computed as the relative displacement between points C and D in the finite element mesh — Fig. 12(a). This variable is the one showing more experimental scatter and worse agreement with the experimental results. The numerical results display the expected dependency with respect to the data sets of the oxides 1 and 2, and so we focus on the results for *Oxide* 2, which gave the best fit for the previously analyzed results. The numerical curve displays an initial descent down to about 5 μm and then a continuous rise, but, overall, the numerical curve lies rather far from the experimental one in most of its range. In fact only one specimen, out of four, shows an initial descent of the inner diameter. A simple elastic model is used next to decouple the volumic change from the ovalization.

4.4. Discussion on the ovalization of the tube

Consider a thin-walled tube or ring subjected to horizontal and vertical external compressive stresses p_1 and p_2 as shown in Fig. 13, with horizontal and vertical defined by Fig. 12(a). It is immediate to see that, if we decompose the loading into hydrostatic part I and deviatoric part II as shown, then the hydrostatic state implies change of volume without ovalization, while the deviatoric state produces ovalization without any change in volume. Thus we can consider the hydrostatic pressure p as the driving force for the capillary height increase, and the deviatoric pressure q as the driving force for the ovalization. With the help of the results in Table 9.2 of Young and Budynas (2002), we can compute p as being proportional to the capillary height increase, and then compute q from the measured change of diameter. The corresponding equations read

$$p = \frac{ED_{\text{cap}}^2 t}{D_i^2 \overline{D}(1-\alpha)} \frac{\Delta H}{L}, \quad q = \eta\left[2E\frac{t}{\overline{D}}\frac{\Delta D_1}{D_i} + (1-\alpha)p\right] \tag{8}$$

where E is the elastic modulus of steel, D_{cap} the inner diameter of the capillary, t, D_i, $\overline{D}$ and L the thickness, inner diameter, mean diameter and effective length of the steel tube, respectively, ΔD_1 the variation of inner diameter measured in the experiments, and the constants α and η are given by,

$$\alpha = \frac{t^2}{3\overline{D}}, \quad \eta = \frac{6\alpha}{1-\alpha+8\alpha F(1+\nu)} \tag{9}$$

and $F = 5/6$ for a tube, and ν is the steel Poisson's ratio (Young and Budynas, 2002). Inserting the values of the parameters, with $E = 200$ GPa, and $\nu = 0.3$, we finally get

$$p = 0.1049\Delta H, \quad q = 6.399\Delta D_1 + .005496p \tag{10}$$

with p and q in MPa and ΔH and ΔD_1 in mm. Thus, the curves in Fig. 12(c) and (d) can be replotted as curves of nominal hydrostatic and deviatoric pressures as shown in Fig. 14. The curves

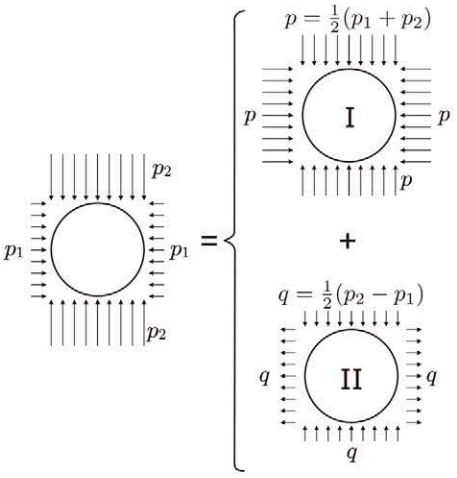

Fig. 13. Sketch of the decomposition of a non-hydrostatic loading into hydrostatic and deviatoric parts.

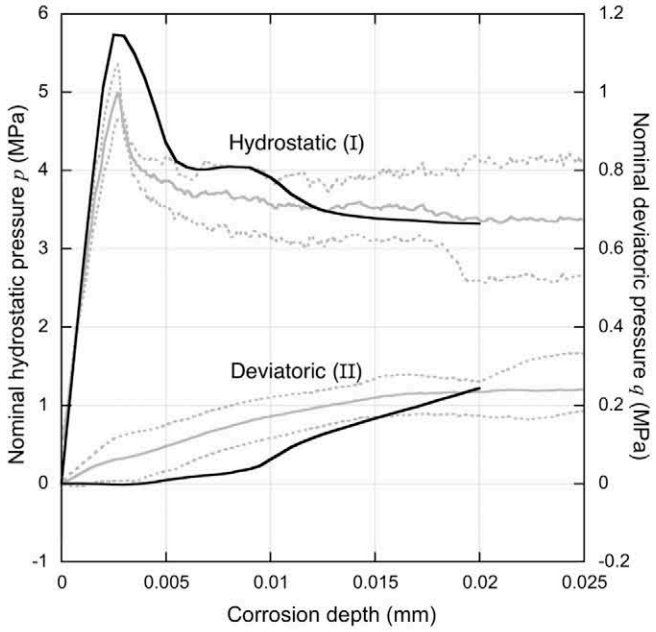

Fig. 14. Plots of hydrostatic and deviatoric components of the nominal pressure for the experimental results (gray curves) and the numerical results for *Oxide* 2. Note the difference in the scales.

corresponding to the nominal hydrostatic pressure are identical to those in Fig. 12(d) except for a change in the vertical scale. The curves corresponding to the purely deviatoric part are easier to interpret than the direct plots of the variation of inner diameter. We observe, first of all, that the numerical response displays a very small deviatoric pressure up to corrosion depths of about 5 μm, while the mean measured deviatoric pressure monotonically increases from the beginning. This seems to indicate that the numerical model is excessively symmetric, which may be due either to a slight mechanical anisotropy of the concrete, or to an excessive simplification when assuming that the corrosion depth is uniform, or both. The second observation, however, is that the mean deviatoric pressure is always a small fraction (less than 7%) of the mean hydrostatic pressure, and thus, minor modifications of the material model or the corrosion depth distribution would be enough to fit the experimental results, for which further work is in progress.

5. Conclusions

A novel implementation of the commonly used impressed current technique in concrete reinforcement corrosion has been presented in which concrete prisms are reinforced with a steel tube instead of a bar. This, together with a special instrumentation of the tubes, permitted to capture some aspects of cracking of concrete that otherwise could not be measured, and that will help in getting a closer view of the mechanics of the corrosion process in conjunction with numerical models. From the results described in the body of the paper, the following conclusions can be drawn:

1. The main crack opening (or an experimental approximation of it) is basically controlled by the oxide net expansion factor β. The shear stiffness of the oxide layer and the tail of the softening curve have a minor influence on the main crack opening.
2. With a net expansion factor $\beta = 2$ and mechanical properties of concrete determined in independent tests, the numerical model follows well the experimental results for the crack opening for the first part of the curve, including the crack formation but it does not capture the curvature displayed by the experimental curves. This can be explained by time-dependent effects, including the possibility of intrusion of the oxide inside the porous network of the concrete, thus leading to an effective β factor which decreases in time (and also with corrosion depth in these constant-current tests).
3. The measurement of the change of the inner volume of the tube and of one of its inner diameters indicates a small, but sensible, ovalization of its cross section. It has been reinterpreted in terms of nominal hydrostatic and deviatoric pressures, which are not to be confused with the actual stresses, but are the stresses that would produce the same observed displacements in a ring of rectangular cross section.
4. The main trend in the experimental nominal hydrostatic pressure is well captured by the numerical model when, keeping $\beta = 2$, the shear stiffness of the oxide is set to 0.001 times the value of the normal stiffness. The effect of the tail of the softening curve also helps in getting a better fit. However, there are slight differences between the peak of the numerical and the experimental curves, which would be greatly reduced by small adjustments of the concrete strength and fracture energy, which are justified by the large difference between the rate of loading in the corrosion tests and in the standard characterization tests.
5. The nominal deviatoric pressure, which does not produce any change in volume, but a pure ovalization, is the effect for which the experimental and the numerical trends differ qualitatively the most. It seems that the numerical model is excessively hydrostatic (i.e., axisymmetric) in the initial part of the test. This is probably due to excessive simplifications in the model: the behavior of concrete is not really fully isotropic (the casting direction is an issue), and the corrosion depth is probably not uniform. However, the magnitude of the deviatoric pressure is much less than that of the hydrostatic pressure, and the mismatch may be considered *minor* in the overall behavior.

Acknowledgments

The authors gratefully acknowledge the *Secretaría de Estado de Investigación, Desarrollo e Innovación* of the Spanish *Ministerio de Economía y Competitividad* for providing financial support for this work under Grant BIA2010-18864. The authors also acknowledge *Oficemen, Grupo Cementos Portland Valderribas* for donating the cement used to fabricate the specimens of this work, Mr. Alois Lehnertz for his major contribution in the design of the electrical sources used in this work and Mr. José Miguel Martínez for his help in fabricating them.

References

Alonso, C., Andrade, C., Rodríguez, J., Díez, J.M., 1998. Factors controlling cracking of concrete affected by reinforcement corrosion. Mater. Struct. 31 (7), 435–441. http://dx.doi.org/10.1007/BF02480466.

Andrade, C., Alonso, C., Molina, F.J., 1993. Cover cracking as a function of bar corrosion: Part I – Experimental test. Mater. Struct. 26 (8), 453–464. http://dx.doi.org/10.1007/BF02472805.

Andrade, C., Alonso, C., Rodríguez, J., García, M., 1996. Cover cracking and amount of rebar corrosion: importance of the current applied in accelerated tests. In: Dhir, R.K., Jones, M.R. (Eds.), Concrete in the Service of Mankind, Concrete repair, rehabilitation and protection. E&FN Spon, London, UK, ISBN 0 419 21490 9, pp. 263–273.

ASTM-Standard-C39, 1986. Standard Test Method for Compressive Strength for Cylindrical Concrete Specimens. ASTM International, West Conshohocken, PA, http://dx.doi.org/10.1520/C0039_C0039M.

ASTM-Standard-C496, 1990. Standard Test Method for Splitting Tensile Strength of Cylindrical Concrete Specimens. ASTM International, West Conshohocken, PA, http://dx.doi.org/10.1520/C0496_C0496M-11.

ASTM-Standard-G1, 2003. Standard Practice for Preparing, Cleaning and Evaluating Corrosion Test Specimens. ASTM International, West Conshohocken, PA, http://dx.doi.org/10.1520/G0001-03R11.

Bazant, Z.P., Gettu, R., 1992. Rate effects and load relaxation in static fracture of concrete. ACI Mater. J. 89 (5), 456–468. http://dx.doi.org/10.14359/2400.

Bazant, Z., Planas, J., 1998. Fracture and size effect in concrete and other quasibrittle materials. C.R.C Press, Boca Raton, FL, ISBN 9780849382840.

Bhargava, K., Ghosh, A.K., Mori, Y., Ramanujam, S., 2006. Model for cover cracking due to rebar corrosion in RC structures. Eng. Struct. 28 (8), 1093–1109. http://dx.doi.org/10.1016/j.engstruct.2005.11.014.

Caré, S., Raharinaivo, A., 2007. Influence of impressed current on the initiation of damage in reinforced mortar due to corrosion of embedded steel. Cem. Concr. Res. 37 (12), 1598–1612. http://dx.doi.org/10.1016/j.cemconres.2007.08.022.

Caré, S., Nguyen, Q.T., L'Hostis, V., Berthaud, Y., 2008. Mechanical properties of the rust layer induced by impressed current method in reinforced mortar. Cem. Concr. Res. 38 (8–9), 1079–1091. http://dx.doi.org/10.1016/j.cemconres.2008.03.016.

Caré, S., Nguyen, Q.T., Beddiar, K., Berthaud, Y., 2010. Times to cracking in reinforced mortar beams subjected to accelerated corrosion tests. Mater. Struct. 43 (1–2), 107–124. http://dx.doi.org/10.1617/s11527-009-9474-2.

Elices, M., Guinea, G.V., Gomez, J., Planas, J., 2002. The cohesive zone model: advantages, limitations and challenges. Eng. Fract. Mech. 69 (2), 137–163. http://dx.doi.org/10.1016/S0013-7944(01)00083-2.

El Maaddawy, T., Soudki, K., 2003. Effectiveness of impressed current technique to simulate corrosion of steel reinforcement in concrete. J. Mater. Civ. Eng. 15 (1), 41–47. http://dx.doi.org/10.1061/(ASCE)0899-1561(2003)15:1(41).

EN-10305-1, 2010. Steel tubes for precision applications. Technical delivery conditions. Seamless cold drawn tubes. European Committee for Standardization. ISBN: 978 0 580 67397 9.

EN-197-1, 2000. Cement – Part 1: Composition, specifications and conformity criteria for common cements. European Committee for Standardization. ISBN: 978 0 580 76786 9.

Fathy, A.M., Sanz, B., Sancho, J.M., Planas, J., 2008. Determination of the bilinear stress-crack opening curve for normal- and high-strength concrete. Fatigue Fract. Eng. Mater. Struct. 31 (7), 539–548. http://dx.doi.org/10.1111/j.1460-2695.2008.01239.x.

Geuzaine, C., Remacle, J.-F., 2009. GMSH: a three-dimensional finite element mesh generator with built-in pre- and post-processing facilities. Int. J. Numer. Methods Eng. 79 (11), 1309–1331. http://dx.doi.org/10.1002/nme.2579.

Guinea, G.V., Planas, J., Elices, M., 1994. A general bilinear fitting for the softening curve of concrete. Mater. Struct. 27 (2), 99–105. http://dx.doi.org/10.1007/BF02472827.

Hillerborg, A., Modéer, M., Petersson, P., 1976. Analysis of crack formation and crack growth in concrete by means of fracture mechanics and fracture elements. Cem. Concr. Res. 6 (6), 773–781. http://dx.doi.org/10.1016/0008-8846(76)90007-7.

Kayafas, I., 1980. Technical note: corrosion product removal from steel fracture surfaces for metallographic examination. Corrosion 36 (8), 443–445. http://dx.doi.org/10.5006/0010-9312-36.8.443.

Mehta, P.K., Monteiro, P.J.M., 2006. Concrete: Microstructure, Properties and Materials, third ed. McGraw-Hill, ISBN 978-0-07-146289-1.

Michel, A., Pease, B.J., Geiker, M.R., Stang, H., Olesen, J.F., 2011. Monitoring reinforcement corrosion and corrosion-induced cracking using non-destructive X-ray attenuation measurements. Cem. Concr. Res. 41 (11), 1085–1094. http://dx.doi.org/10.1016/j.cemconres.2011.06.006.

Molina, F., Alonso, M., Andrade, C., 1993. Cover cracking as a function of bar corrosion: Part II – Numerical model. Mater. Struct. 26 (9), 532–548. http://dx.doi.org/10.1007/BF02472864.

Nguyen, Q.T., Caré, S., Berthaud, Y., Millard, A., Ragueneau, F., 2011. Experimental and numerical behaviour of reinforced mortar plates subjected to accelerated corrosion. Int. J. Numer. Anal. Methods Geomech. 35 (10), 1141–1159. http://dx.doi.org/10.1002/nag.947.

Pease, B.J., Michel, A., Thybo, A., Stang, H., 2012. Estimation of elastic modulus of reinforcement corrosion products using inverse analysis of digital image correlation measurements for input in corrosion-induced cracking model. In: Sixth International Conference on Bridge Maintenance, Safety and Management (IAMBAS), Lake Como, Italy.

Planas, J., Guinea, G.V., Elices, M., 1999. Size effect and inverse analysis in concrete fracture. Int. J. Fract. 95 (1–4), 367–378. http://dx.doi.org/10.1023/A:1018681124551.

Planas, J., Elices, M., Guinea, G.V., Gomez, F.J., Cendon, D.A., Arbilla, I., 2003. Generalizations and specializations of cohesive crack models. Eng. Fract. Mech. 70 (14), 1759–1776. http://dx.doi.org/10.1016/S0013-7944(03)00123-1.

Planas, J., Guinea, G.V., Galvez, J.C., Sanz, B., Fathy, A.M., 2007. Report 39: Experimental Determination of the Stress-Crack Opening Curve for Concrete in Tension – Final report of RILEM Technical Committee TC 187-SOC. RILEM Publications SARL, Ch. 3. Indirect tests for stress-crack opening curve, pp. 13–29. ISBN:978-2-35158-049-3.

Sánchez, P.J., Huespe, A.E., Oliver, J., Toro, S., 2010. Mesoscopic model to simulate the mechanical behavior of reinforced concrete members affected by corrosion. Int. J. Solids Struct. 47 (5), 559–570. http://dx.doi.org/10.1016/j.ijsolstr.2009.10.023.

Sancho, J.M., Planas, J., Cendon, D.A., Reyes, E., Galvez, J.C., 2007a. An embedded cohesive crack model for finite element analysis of concrete fracture. Eng. Fract. Mech. 74 (1–2), 75–86. http://dx.doi.org/10.1016/j.engfracmech.2006.01.015.

Sancho, J.M., Planas, J., Fathy, A.M., Gálvez, J.C., Cendón, D.A., 2007b. Three-dimensional simulation of concrete fracture using embedded crack elements without enforcing crack path continuity. Int. J. Numer. Anal. Methods Geomech. 31 (2), 173–187. http://dx.doi.org/10.1002/nag.540.

Sanz, B., Planas, J., Fathy, A.M., Sancho, J.M., 2008. Modelización con elementos finitos de la fisuración en el hormigón causada por la corrosión de las armaduras. Anales de Mecánica de la Fractura 25 (2), 623–628, ISBN: 0213-3725.

Sanz, B., Planas, J., Sancho, J.M., 2013. An experimental and numerical study of the pattern of cracking of concrete due to steel reinforcement corrosion. Eng. Fract. Mech. 114, 26–41. http://dx.doi.org/10.1016/j.engfracmech.2013.10.013.

Tuutti, K., 1982. Corrosion of steel in concrete. CBI Forskning 82:4. Swedish Cement and Concrete Research Institute. ISBN:0346-6906.

Young, W.C., Budynas, R.G., 2002. Roark's Formulas for Stress and Strain, 7th Edition. McGraw-Hill, ISBN 0-07-072542-X.